

Tunable self-assembled Casimir microcavities and polaritons

Timur Shegai (✉ timurs@chalmers.se)

Chalmers University of Technology <https://orcid.org/0000-0002-4266-3721>

Battulga Munkhbat

Chalmers University of Technology <https://orcid.org/0000-0002-1923-0960>

Adriana Canales

Chalmers University of Technology

Betül Küçüköz

Chalmers University of Technology

Denis Baranov

Chalmers University of Technology <https://orcid.org/0000-0002-8071-1587>

Physical Sciences - Article

Keywords: self-assembly, self-ordering, Casimir microcavities

Posted Date: March 24th, 2021

DOI: <https://doi.org/10.21203/rs.3.rs-334398/v1>

License:   This work is licensed under a Creative Commons Attribution 4.0 International License.

[Read Full License](#)

Version of Record: A version of this preprint was published at Nature on September 8th, 2021. See the published version at <https://doi.org/10.1038/s41586-021-03826-3>.

Tunable self-assembled Casimir microcavities and polaritons

Battulga Munkhbat,¹ Adriana Canales,¹ Betül

Küçüköz,¹ Denis G. Baranov,^{1,2} and Timur Shegai^{1,*}

¹*Department of Physics, Chalmers University of Technology, 412 96, Göteborg, Sweden*

²*Center for Photonics and 2D Materials,*

Moscow Institute of Physics and Technology, Dolgoprudny 141700, Russia

Abstract

Spontaneous formation of ordered structures – self-assembly – is ubiquitous in nature and observed on different length scales, ranging from atomic and molecular systems to micro-scale objects and living matter. Self-ordering in molecular and biological systems typically involves short-range hydrophobic and van der Waals interactions. Here, we introduce an approach to micro-scale self-assembly based on the joint action of attractive Casimir and repulsive electrostatic forces arising between charged metallic nanoflakes in a solution. This system forms a self-assembled optical Fabry-Pérot microcavity with a fundamental mode in the visible range (long-range separation distance $\sim 100\text{-}200$ nm) and a tunable equilibrium configuration. Furthermore, by placing an excitonic material in the microcavity region, we are able to realize hybrid light-matter states (polaritons), whose properties, such as the coupling strength and the eigenstate composition, can be controlled in real time by the concentration of ligand molecules in the solution and light pressure. These Casimir microcavities can find future use as sensitive and tunable platforms for a variety of applications, including opto-mechanics, nanomachinery, and cavity-induced polaritonic chemistry.

In 1948 Hendrik Casimir elucidated on the nature of attractive forces between two parallel uncharged perfect electric conductor plates in vacuum, later named after him [1]. These forces have quantum origins and exist even in the absence of any external charges or fields. They appear even at zero temperature as a consequence of zero-point charge fluctuations [2]. In parallel with Casimir work, a related theory of colloidal stability – the so-called DLVO theory (after Derjaguin, Landau, Verwey and Overbeek) – was developed [3, 4]. The main ingredients of this theory are attractive van der Waals and repulsive electrostatic forces. In water solution, the latter are characterized by the double layer potential and Debye-Hückel screening length (κ^{-1}). Later, Lifshitz and colleagues demonstrated a deep intrinsic relationship between Casimir and van der Waals forces, as well as extended their applicability to a space filled by a medium [5, 6]. Historically, the van der Waals interactions have been associated with short-range separation distances, while Casimir with long-range distances (where retardation corrections are important) [5, 6].

Casimir forces were successfully measured in several configurations using, for instance, two chromium mirrors, a torsion pendulum, microresonators, and gold spheres [7–10]. However, a similar Casimir problem may arise not only in a sterile vacuum environment, as was studied in these earlier experiments, but also in a crowded water solution, such as a suspension of chemically synthesized metallic nanoflakes. In this case, Casimir forces can lead to self-assembly.

Here, we make use of the combined Casimir and electrostatic interactions in gold nanoflake colloid systems as a means to realize self-assembled and tunable microcavities. Such microcavities can serve as a useful platform for studying self-assembly in general, and the complexity of interactions behind it in particular [11]. Moreover, the self-assembled structures form a Fabry-Pérot microcavity with the fundamental optical mode in the visible spectral range, allowing for a facile readout of the equilibrium distance by transmission or reflection spectroscopy. The resulting equilibrium distance between the flakes can be controlled by the concentration of ligand molecules in the solution, temperature, and light pressure, which allows for active tuning of the cavity resonance by external stimuli.

Furthermore, as a proof-of-principle application of our approach, we use these microcavities for realization of cavity-exciton hybrid states – polaritons. Polaritons emerge as a result of strong coupling between an optical mode and a material resonance, and are frequently realized in molecular or solid-state platforms that require accurate nano-fabrication

and lack simple means for tunability [12–19]. Using the self-assembly approach, we realize polaritons by placing an excitonic medium in the microcavity region, as well as observe their laser-induced on-demand modulations in and out of the strong coupling regime.

In a broader perspective, our work shows that Casimir interaction greatly affects self-assembly and leads to emergence of useful Fabry-Pérot microcavity resonances. This suggests a number of future applications, including a sensitive and tunable room-temperature platform for opto-mechanics [20], nanomachinery [21], and polaritonic chemistry [22].

Basic principle

Fig. 1a illustrates the basic mechanisms enabling self-assembled microcavities: a water solution of cetyltrimethylammonium bromide ligand molecules (CTAB) hosts floating gold nanoflakes. When two flakes approach each other, two types of interaction emerge between them. The Casimir interaction is attractive and caused by the vacuum fluctuations of the electromagnetic field in the cavity formed between the flakes, the electrostatic interaction is repulsive and caused by the formation of electric double layers around the flakes. Therefore, the joint action of the two interactions may result in the existence of a stable equilibrium (a discussion about possible additional contributions to the interactions between nanoflakes is given in Note S1).

To illustrate the formation of a stable equilibrium, we calculate the total potential of the system per unit area U_0 (see Methods) as a function of the separation L between two charged metallic nanoflakes for a fixed net surface charge density $\sigma = 1 \text{ mC/m}^2$ (equivalent to ≈ 0.6 electrons per 100 nm^2) and for a series of ligand concentrations C in the solution, Fig. 1b. In the left-most scenario calculated for a relatively low ligand concentration $C = 0.35 \text{ mM}$ the electrostatic repulsion dominates leading to no stable equilibrium at short distances. In the middle plot, calculated for $C = 0.7 \text{ mM}$, a local potential minimum appears at about 105 nm separation between the charged flakes. This arrangement gives rise to an optical cavity with a resonant wavelength in the visible range. Finally, for even higher ligand concentration $C = 1.4 \text{ mM}$, the local potential minimum disappears, leaving only a trivial minimum at $L = 0$. Thus, a joint action of repulsive electrostatic and attractive Casimir forces is theoretically shown to lead to a stable equilibrium at $L \approx 100 \text{ nm}$ for realistic parameter values of σ and C . We note that the predicted stable equilibrium distance

significantly exceeds the corresponding Debye-Hückel lengths $\kappa^{-1} = 10\dots 25$ nm, indicating that electrostatic repulsion must be strongly screened to reach the level of attractive Casimir forces (see Note S1 and Fig. S8C).

Nanoflake dimers

To realize a stable Casimir microcavity experimentally, as shown schematically in Fig. 1a, we use chemically synthesized gold nanoflakes. Single crystalline gold nanoflakes (Fig. 1d), with average thicknesses of 34 ± 10 nm and a few microns in lateral dimensions, were synthesized using a rapid and seedless wet chemical method in an aqueous solution (see Methods) [23]. A freshly-prepared gold nanoflake solution, containing CTAB (~ 0.35 mM), was drop-casted onto a thin glass coverslip. The droplet was encapsulated by another coverslip using a thin polydimethylsiloxane (PDMS) spacer, to prevent evaporation of the liquid. After drop-casting, the non-aggregated nanoflakes slowly sediment towards the glass substrate, where they diffuse laterally due to Brownian motion until eventually colliding with another individual flake or aggregate. In the simplest scenario, two isolated nanoflakes diffuse close to one another at a distance where the attraction becomes relevant and form a stable nanoflake pair (see Fig. 1d and and supplementary movie S1). This self-assembled dimer is at the same time a Fabry-Pérot microcavity, whose equilibrium distance can be controlled by the concentration of ligand molecules in water solution, temperature, and light pressure. Once formed, such self-assembled microcavities remain stable for indefinitely long times (in this study we have monitored their stability over the period of a few weeks without noticeable resonance degradation).

Since the surfaces of both flakes in a dimer are charged by the same ions, the electrostatic interaction between the flakes should be repulsive. Yet, they form stable dimers, which implies that a compensating attractive force must act. This force can be either of gravitational, electromagnetic, hydrodynamic, or entropic origin (the analysis of possible attractive forces is given in Note S1). In what follows, we assume a joint action of electrostatic and Casimir potentials and neglect other possible contributions. Our theoretical analysis and control experiments support this hypothesis (Note S1 and Figs. S2-3).

To assess the optical characteristics of the self-assembled cavities, we performed normal incidence reflection spectroscopy using an oil immersion $100\times$ objective (Nikon, NA = 0.5),

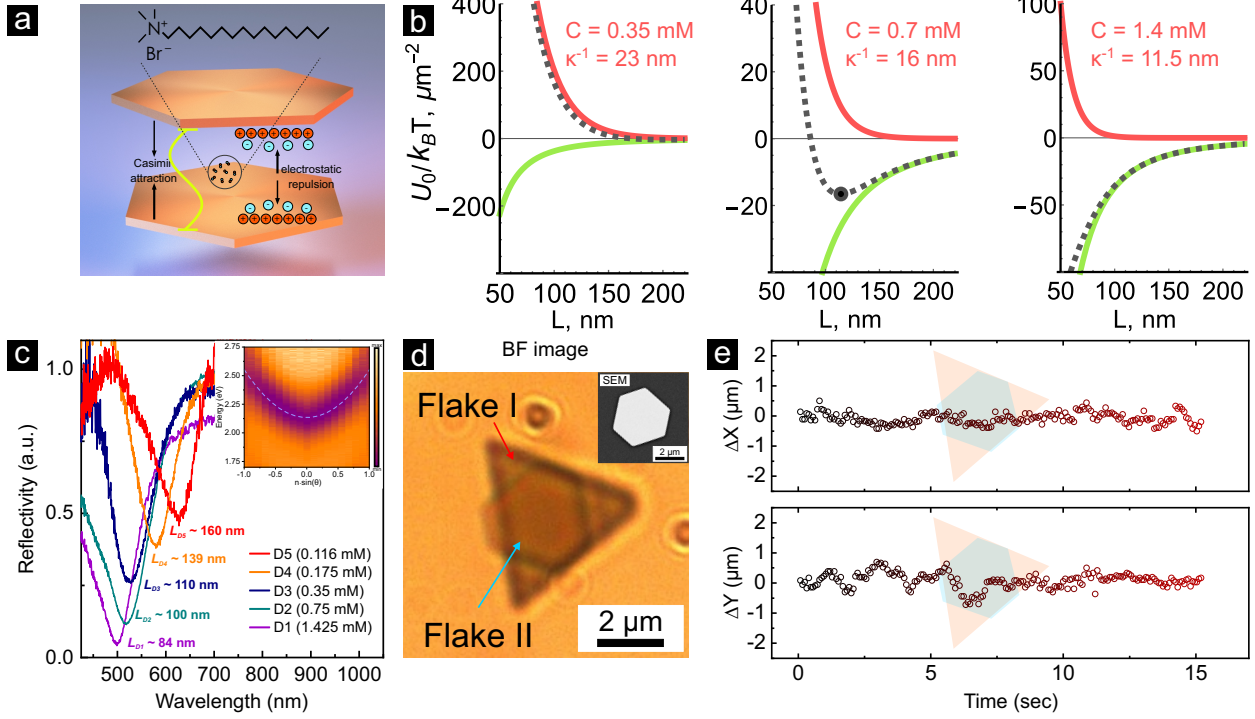


FIG. 1. The self-assembled microcavity system and the physical mechanism behind its operation. (a) Sketch of the system: two parallel gold flakes floating in a water solution of a ligand (CTAB). The two flakes are in a metastable equilibrium at a distance L_{cav} from each other thanks to the joint action of the attractive Casimir force and the repulsive electrostatic force. (b) Calculated total potential (sum of the Casimir and electrostatic potentials) U_0 per unit area of the system of two 30 nm thick gold flakes in a CTAB water solution with the fixed surface charge density $\sigma = 1 \text{ mC/m}^2$ and different salt concentrations – 0.35, 0.7, and 1.4 mM, respectively. Total, electrostatic, and Casimir potentials are plotted as dotted, red, and green lines, respectively. (c) Quasi-normal incidence reflectivity of the self-assembled cavities with $L_{cav} \approx 84 \text{ nm}$ (purple), 100 nm (blue-green), 110 nm (blue), 139 nm (orange), and 160 nm (red), respectively. Different cavity thicknesses are obtained by varying the CTAB concentrations of $C_{CTAB} = 1.425, 0.75, 0.35, 0.175$ and 0.116 mM , correspondingly. Inset: Angle-resolved reflection of an exemplary self-assembled microcavity with $L_{cav} \approx 148 \text{ nm}$ exhibiting a characteristic parabolic behavior. (d) Bright-field image of a self-assembled dimer. Inset: SEM image of an exemplary gold nanoflake. (e) Relative displacement between top and bottom nanoflakes within the dimer shown in (d) along x and y directions as a function of time. Note that while flakes can move with respect to each other, their relative displacement is always small in comparison to the lateral size of the flakes.

directed to a fiber-coupled spectrometer (see Methods). These measurements were performed on several microcavities formed in CTAB solutions of different concentrations (Fig. 1c). To ensure reproducibility, we recorded reflectivity spectra from dozens of samples in the solution (data available upon request).

Fig. 1c shows reflection spectra collected from five representative samples with different $C_{CTAB} = 1.425, 0.75, 0.35, 0.175$ and 0.116 mM, that were obtained by mixing the stock solution (0.35 mM) with different amounts of either pure de-ionized water or with a known concentration of CTAB solution (see Note S2 for determining the CTAB concentration of the stock solution). The spectra reveal a number of reflection dips, which correspond to Fabry-Pérot modes of the self-assembled microcavities. Fitting the data with the transfer-matrix method allows us to extract the equilibrium thicknesses of the cavities; the fitting yields L_{eq} of $\sim 84, 100, 110, 139,$ and 160 nm for dimers D1-D5, respectively (see Fig. S7).

The developed picture of the Casimir-electrostatic potential can be used to analyze the observed equilibrium configurations and estimate the surface charge density accumulated on the Au nanoflakes. To that end, for each independently known CTAB concentration we varied the surface charge density until the equilibrium separation predicted by the Casimir-electrostatic potential matched the one extracted from the measured reflection spectra (see Fig. S7). The results of this analysis suggest that the net surface charge density σ lies in the range $\sim 0.1...2$ mC/m² (equivalent to less than 1 electron per area of 100 nm²), and grows linearly with CTAB concentration, Fig. S8. This observation is in line with the previously reported linear dependence of the ζ -potential of gold colloids on CTAB concentration below the critical micelle point [24, 25]. The relatively low magnitudes of the charge densities (much lower than the surface density of CTAB itself) are probably due to formation of the electric double layer and co-adsorption of Br^- , which effectively screens the presence of positive CTA^+ ions at the surface [26].

Furthermore, we performed angle-resolved reflectivity measurements using an inverted optical microscope equipped with an oil-immersion objective ($100\times$, $\text{NA} = 1.3$). The dispersion reflectivity plot is shown in the inset of Fig. 1c and exhibits a characteristic of parabolic dispersion, which confirms the flat Fabry-Pérot microcavity formation. More examples of dispersion plots are shown in Fig. S11.

To demonstrate that self-assembled microcavities are stable not only in the vertical direction, but also laterally, we tracked the trajectories of the top and bottom nanoflakes within a

dimer over time (Fig. 1E). The cavity as a whole is diffusing in the solution due to Brownian motion. However, the flakes are free to move with respect to each other (both translationally and rotationally) and their relative displacement is always small (submicron) in comparison to the lateral size of the flakes (several microns), Fig. 1E and supplementary movie S2. This behavior is remarkable, since the nanoflakes within a dimer should be electrostatically repelled in the lateral direction. Yet, they follow each other for indefinitely long times, which can only occur if the electrostatic repulsion is balanced by an attractive interaction of non-electrostatic nature. This attractive interaction is likely related to the edge effects and to the lateral Casimir force, which is an important finding, since observations of lateral Casimir forces are usually more challenging than vertical ones [27] (numerical analysis of the lateral Casimir force goes beyond this study [28, 29]).

Nanoflake trimers

The process of self-assembly does not stop at the point of dimer formation: a dimer can collide with another flake in the solution and form a stable trimer, as illustrated in Fig. 2a. The probability of this process depends on the concentration of nanoflakes in the solution and inter-flake interactions strengths, which allows controlling the relative population of dimers, trimers, and higher-order aggregates, in a manner similar to previously reported self-limiting aggregation of silver nanoparticle colloids [30].

For a quantitative characterization we chose the simplest case of a multi-stack system – a trimer (higher-order aggregates are shown in Fig. S13). We collected normal incidence reflection spectra from several trimers, Fig. 2b. Just like in the case of dimers, trimers form a stable aggregate both vertically and laterally (see supplementary movie S3-S4 and Fig. S14).

Trimers exhibit characteristic double-dip reflection spectra (see Fig. 2b-c). The origin of this double-dip behavior lies in the interaction of Fabry-Pérot modes hosted by each cavity separated by the semi-transparent middle mirror. The electromagnetic mode hosted by one of the cavities interacts with the other half of the system at a rate determined by the middle semi-transparent mirror. This results in symmetric and anti-symmetric hybrid eigenmodes with the splitting between the two determined by the thickness of the middle mirror. This view is similar to the symmetric and anti-symmetric polariton branches in the Rabi-like

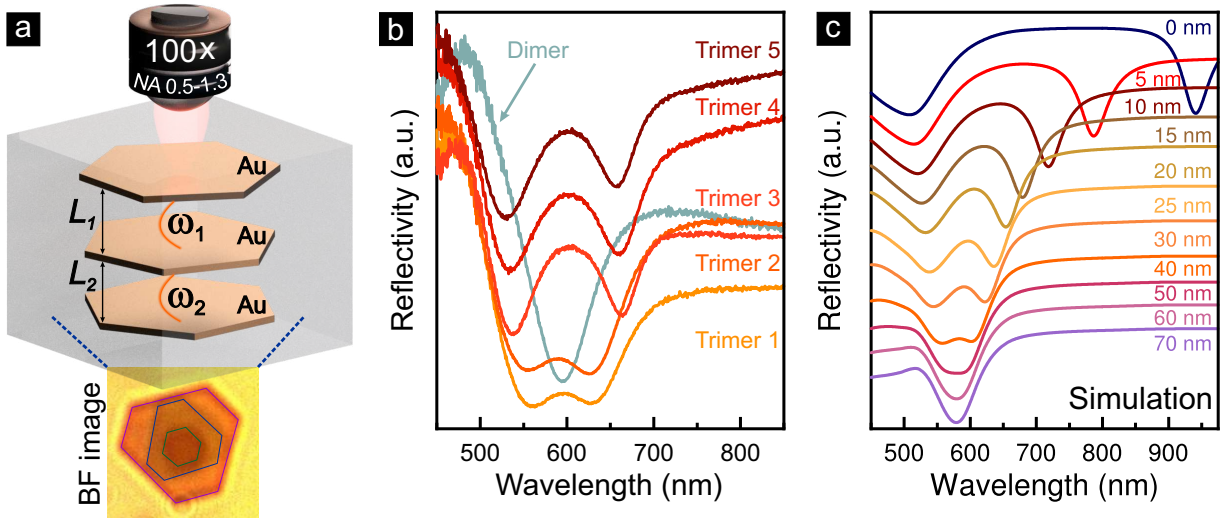


FIG. 2. **Self-assembled trimer cavities** (a) Sketch of the self-assembled trimer system. (b) Quasi-normal incidence reflectivity spectra for several self-assembled trimers with various geometrical characteristics. The grey-blue curve shows the reflectivity spectrum of a dimer for comparison. (c) Calculated reflectivity spectra of three parallel gold flakes as a function of the thickness of the middle-mirror (flake).

problem, following which, the three-mirror geometries were recently interpreted in terms of hybrid light-matter polaritonic states [31–33].

To illustrate this mechanism, we analytically calculated normal incidence reflection spectra of a trimer with the middle mirror thickness ranging from 70 nm down to 0 nm, corresponding to completely opaque middle mirror and the absence of the middle mirror, respectively, Fig. 2c. For an optically thick middle mirror, the interaction vanishes and the reflection spectrum exhibits a single dip associated with the Fabry-Pérot eigenmode of the top or bottom cavity. Reducing the middle mirror thickness allows interaction and opens the splitting between the two hybrid modes. The reduction of the middle mirror thickness leads to a monotonic increase in the reflection dip splitting (Fig. 2c), until the lower-energy branch approaches the 1st order, and the higher-energy branch approaches the 2nd order Fabry-Pérot modes of the cavity formed by top and bottom mirrors. This limiting case corresponds to the vanishingly small middle mirror thickness and represents the maximum splitting possible for the three-mirror configuration.

Experimental data in Fig. 2b shows several splitting values, indicating variations in the

middle mirror thicknesses. By fitting the measured spectra with the transfer-matrix method, we extracted the thickness of the middle mirrors and apparent Rabi splittings (see Table S2-S3 and Fig. S15-S16). The range of extracted thicknesses agrees well with the typical values measured by atomic force microscopy $\sim 20 - 30$ nm (see Fig. S17).

Nanoflake on static mirror

Now let us demonstrate an alternative configuration consisting of a single nanoflake in solution floating above a stationary thermally-evaporated gold film (Fig. 3a). Similarly to nanoflake dimer configuration, this approach allows for the formation of self-assembled structures, whose equilibrium is determined by the joint Casimir-electrostatic potential.

Nanoflake-on-static-mirror offers several ways of additional control over the properties of the self-assembled microcavities. These include incorporation of a dielectric (SiO_2) or excitonic (WSe_2) spacer with controllable thickness above the bottom mirror (Fig. 3c), the adjustable thickness of the bottom mirror, the usage of silver nanoflakes as movable mirrors (Fig. S18), and the assessment of the contribution of gravity contribution to the self-assembly mechanism.

We first check the role of gravity on the formation of stable cavities. Fig. 3b shows reflection spectra of a single cavity collected in upside and upside-down configurations. The reflectivity spectra in both cases exhibit dips at around 600 nm, implying the equilibrium distances are the same in both cases. This suggests that gravity plays a minor role in formation of these microcavities, and the equilibrium distance is determined by the interplay of the Casimir attraction and the electrostatic repulsion.

Next we characterized self-assembled cavities in nanoflake-on-static-mirror configuration versus the thickness of the SiO_2 spacer, Fig. 3c. The measured spectra indicate that the reflection dip gradually shifts to longer wavelengths with increasing spacer thickness. The transfer-matrix analysis reveals that the equilibrium thickness of the water layer between the SiO_2 spacer and the nanoflake in this parameter range increases almost linearly with the SiO_2 thickness, Fig. S19. This behavior suggests that the equilibrium water thickness is not a universal constant but a parameter governed by more complicated physics, which should include the influence of Casimir attraction and electrostatic repulsion. Thus, the dielectric spacer allows tuning of the resonant wavelength of self-assembled cavities.

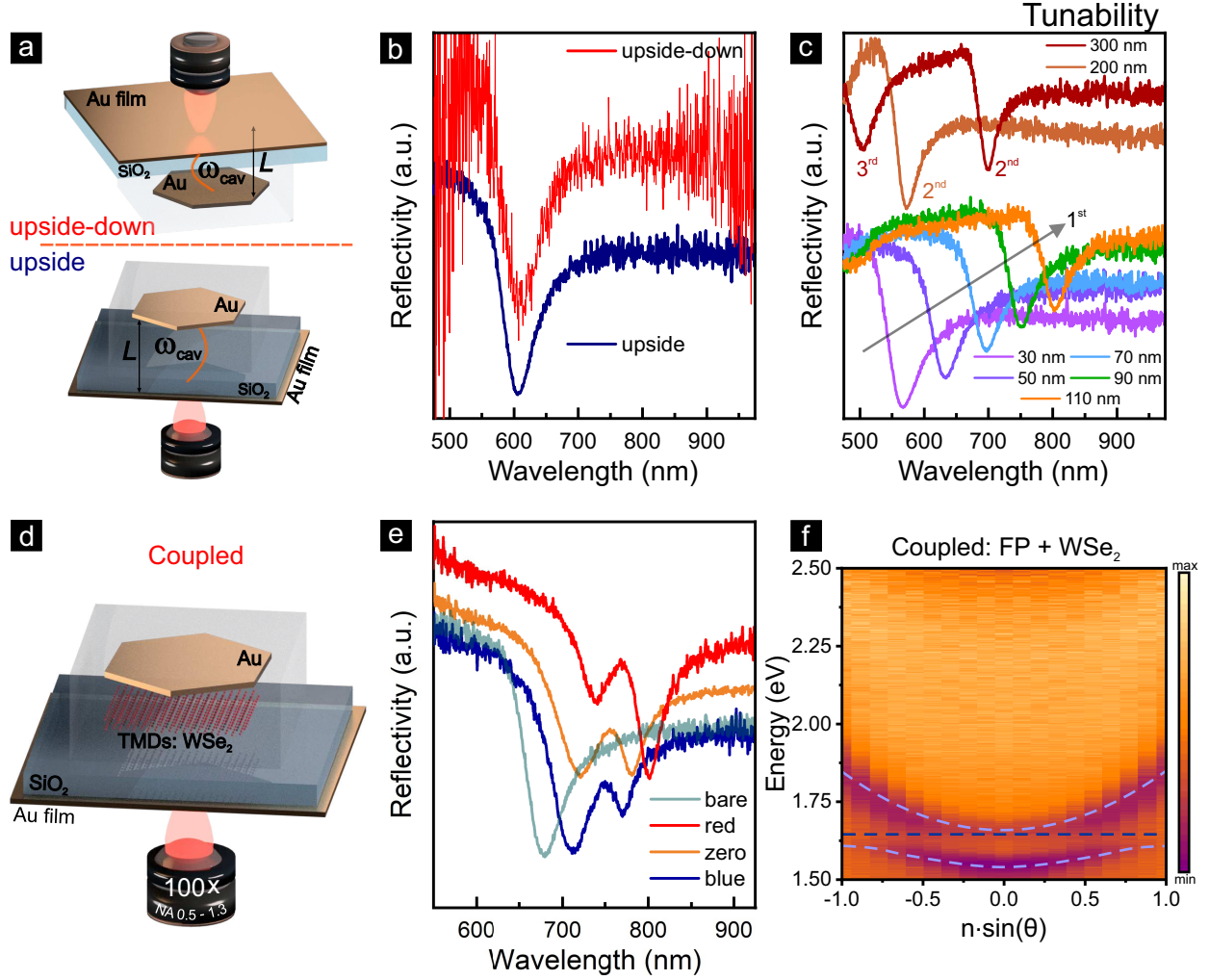


FIG. 3. Self-assembled cavities in nanoflake-on-static-mirror configuration and the formation of polaritons. (a) Sketch of a self-assembled Fabry-Pérot microcavity in nanoflake-on-static-mirror configuration. (b) Quasi-normal incidence reflectivity spectra for the microcavities with upside (blue) and upside-down (red) configurations, respectively. (c) Tuning the resonance of microcavities with various SiO₂ spacers thickness. (d) Sketch of a self-assembled microcavity coupled to few-layers of WSe₂. (e) Quasi-normal incidence reflectivity of the cavity coupled to various thicknesses of few-layer WSe₂, showing pronounced Rabi splitting and correspondingly microcavity-exciton polariton formation. Note that red, orange, and blue curves show various detunings of cavity resonance with respect to the exciton resonance of WSe₂. (f) Dispersion measurement for the polaritonic microcavity loaded with few layer WSe₂, exhibiting a pronounced mode anti-crossing. Dashed lines are guides for the eye.

To quantify the stability of the self-assembled microcavity in the Brownian regime, in Fig. 4c we show the time-resolved evolution (1 frame = 0.02 s) of the equilibrium distance and its average value $\langle L_{cav} \rangle$ of around ~ 177 nm. The standard deviation σ_L (Fig. 4c shows the distribution of the L_{cav} extracted by the transfer matrix method) is only about 1.6 nm, which is rather remarkable for a micron-size self-assembled system at room temperature and in water solution. This value agrees well with the typical standard deviation of the mirror displacement obtained in the stochastic simulations of the cavity dynamics (Fig. S10). The modelling was done for a simpler situation corresponding to nanoflake dimers (see Methods). The simulations yield the vertical displacement deviation of only a few nm from the equilibrium position at room temperature, which stems from the high stiffness of the Casimir-electrostatic potential (see Note S3).

Finally, by introducing an excitonic layer in between the bottom film and the Au flake, the nanoflake-on-static-mirror configuration allows realization of proof-of-principle polaritonic states as mixtures of Fabry-Pérot cavity photons and excitons in the excitonic material. This polariton is self-assembled and tunable. To realize such a scenario experimentally, we choose WSe₂ because of its high oscillator strength and appropriate resonance wavelength of the A-exciton [34]. A few-layer WSe₂ flake was transferred on the SiO₂ spacer covering the gold film (Methods), and subsequently covered by the nanoflake floating in water solution (the lateral trapping of the gold nanoflake in this configuration is enabled by a focused laser beam, which acts as an optical tweezer). Normal incidence reflectivity spectra measured from several such systems show pronounced Rabi splitting (Fig. 3e). The corresponding dispersion measurement for the polaritonic microcavity, loaded with a few layers of WSe₂, exhibits a pronounced mode anti-crossing, which proves the system is in the strong coupling regime (Fig. 3f).

Active tuning

The self-assembled cavity (either in Figs. 1-3) represents a damped optomechanical resonator with the restoring force provided by the Casimir-electrostatic potential, while the hydrodynamic drag produces the friction. As any optomechanical system, it allows tuning the cavity resonance by applying external stimuli. We use modulated laser light to exert a pressure on the nanoflake and displace it from its equilibrium, Fig. 4a (see Methods).

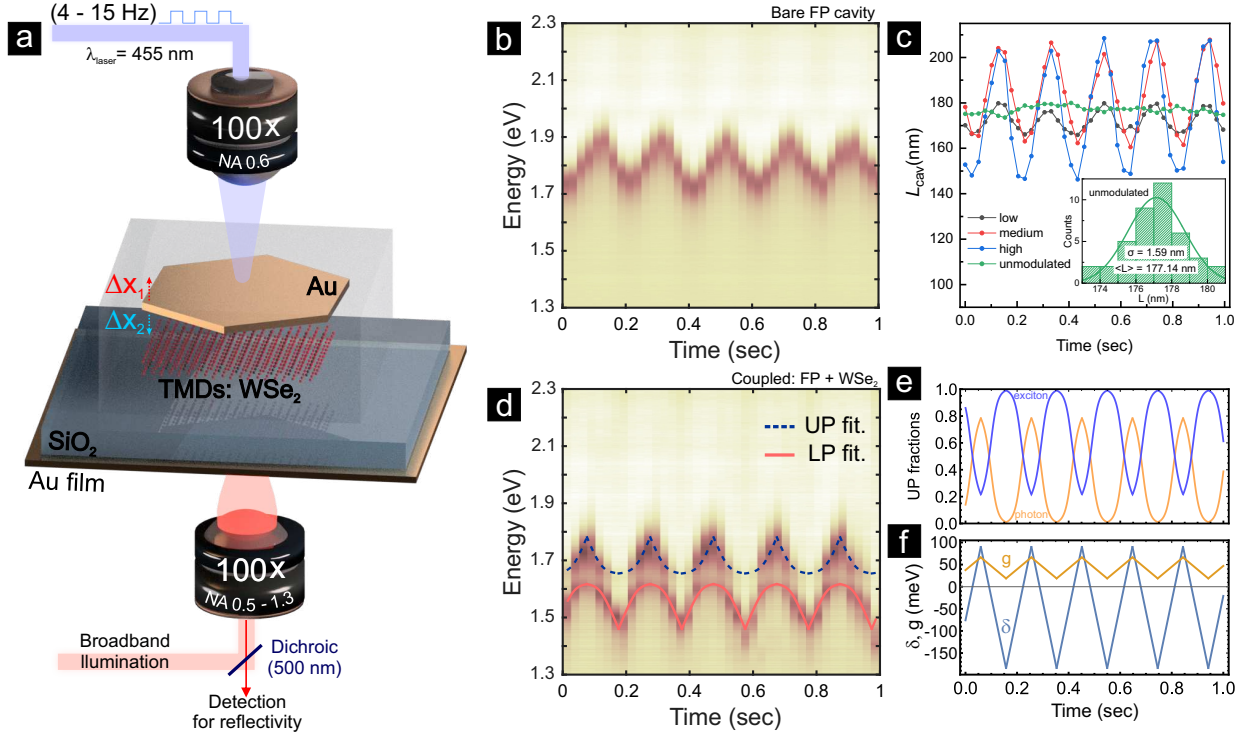


FIG. 4. **Actively tunable microcavities and polaritons.** (a) Schematic of the setup for active tuning of the microcavity by modulating the floating gold flake along vertical direction with a control laser. Time-resolved (b) reflectivity spectra and (c) extracted total thicknesses of empty self-assembled cavities under optical modulation at 5 Hz using low (0.17 kW/cm^2), medium (0.57 kW/cm^2), and high (1.86 kW/cm^2) laser irradiance. (d) Time-resolved reflectivity spectra of the polaritonic system containing a few-layer WSe_2 film inside the Fabry-Pérot cavity. Extracted (e) exciton-photon compositions for upper polariton, and (f) coupling strength (orange) and detuning (grey-blue), respectively.

We start by modulating an empty self-assembled cavity in nanoflake-on-static-mirror configuration. Fig. 4b shows the map of time-resolved reflection spectra (modulated by a mechanical chopper at 5 Hz), revealing a reflection dip oscillating between ~ 1.7 and 1.9 eV with time. This corresponds to vertical displacement of the nanoflake by $\sim \pm 20 \text{ nm}$ with respect to the equilibrium position as the laser is exerted. The reflection as a function of time can be modelled by the transfer-matrix method (see Methods), which allows extracting the vertical displacement quantitatively (Fig. 4c). It is important to mention that the modulation speed and depth depend on the parameters of the laser used

in these experiments, for example, a higher incident intensity can lead to a larger vertical displacement. This behavior is summarized in Note S4 and Figs. S20-S21.

Laser-induced modulation of the cavity resonance can be caused by heating or optical pressure. To reveal the actual reason, we (i) illuminated the system with the modulating laser from below, and (ii) studied the effect of heating the system with the control laser. The result of these two additional experiments, which are summarized in Note S4, strongly suggest that the observed modulation is caused by the radiation pressure of the modulating laser.

The observed laser-induced displacement allows estimating the stiffness of the Casimir-electrostatic potential k in nanoflake-on-static-mirror configuration. For the highest irradiance, the characteristic radiation pressure is $P_{rad} = I_0/c \approx 0.06$ Pa (where I_0 is the laser irradiance and c is the speed of light), which for displacement $\delta x = 20$ nm yields $k = P_{rad}/\delta x \approx 3.1 \times 10^6$ N/m³. This value is within the range obtained for nanoflake dimer configuration (see Fig. S12), which is an important argument for the validity of our estimations. Slightly higher values of the stiffness predicted for dimer configuration can be explained by additional complications in nanoflake-on-static-mirror system, such as the unknown distribution of surface charges in/at the SiO₂ spacer and the electrostatic edge effects.

After modulating the empty Fabry-Pérot cavity, we turn to modulation of the polaritonic system containing a WSe₂ multilayer between the mirrors. Variation of the cavity thickness in this scenario has a two-fold effect: not only does it enable modulation of the bare Fabry-Pérot mode energy, but it also modifies the vacuum field of the cavity, thus affecting the cavity-exciton coupling strength and the composition of the polaritonic eigenstates. Positions of the two reflection minima, corresponding to upper and lower polariton modes, vary in time as seen in Fig. 4d. The reflection minima red-shift by ~ 0.2 eV compared to the empty cavity, which is due to the high background refractive index $n \sim 4$ of WSe₂ [34].

The recorded time-resolved reflection map allows for extracting parameters of the coupled system as it is modulated (additional examples can be found in Fig. S11). To that end, we fit the spectral positions of reflection minima with the eigenvalues of a periodically modulated Jaynes-Cummings Hamiltonian (see Methods). Fig. 4f compares the resulting coupling strength $g(t)$ with the cavity-exciton detuning $\delta(t) = \omega_{cav}(t) - \omega_{exc}(t)$. The Jaynes-Cummings description of any polaritonic system predicts that once the detuning sig-

nificantly exceeds the coupling strength, $|\delta(t)| > g(t)$, the system can be tuned out of the strong coupling regime. Such behavior is clearly visualized in the time-dependent Hopfield coefficients of the system showing nearly 100% photonic or excitonic character of the eigenstates at times corresponding to the minima of $g(t)$. Conversely, at time instances near the maxima of $g(t)$, the eigenstates of the system are polaritonic with nearly equal fractions of the photonic and excitonic components, Fig. 4e.

CONCLUSION

To conclude, we have presented a platform for self-assembled optical microcavities and polaritons enabled by the joint action of the attractive Casimir and repulsive electrostatic interactions. Importantly, the tunable microcavities studied here are highly stable in both the vertical and lateral directions, and exhibit pronounced optical resonances in technologically relevant visible spectral range. The standard deviation of the L_{cav} is as small as 1.6 nm at room temperature, which is on the order of 1% of the equilibrium cavity thickness. The long-term cavity stability is also remarkable, as the resonances remain almost unchanged for as long as they have been monitored (multiple weeks).

Our platform enables not only ordinary Fabry-Pérot microcavities, but also vertical multi-mirror aggregates with complicated modal structure, as well as proof-of-principle realization of polaritonic states when the cavities interact with excitonic material (such as WSe₂). By modulating the system with chopped laser light, we can actively control the polaritonic eigenstates and tune the system in and out of the strong coupling regime. These findings open possibilities for exploring self-assembled Casimir microcavities as sensitive and tunable platforms in opto-mechanics [20], nanomachinery [21], polaritonic chemistry [22], and other promising cavity-induced applications. More generally, our approach expands the toolbox of available self-assembly methods.

Acknowledgments The authors acknowledge Kasper Eliasson for help with Raman measurements. The authors acknowledge financial support from the Swedish Research Council (under VR Miljö project, grant No: 2016-06059; and VR project, grant No: 2017-04545), Knut and Alice Wallenberg Foundation (project No: 2019.0140), and Chalmers Excellence Initiative Nano.

Authors contribution B.M. and T.O.S. conceived the idea. B.M. fabricated the samples. B.M. and A.C. performed optical measurements. B.M. and B.K. investigated active tuning of the structures. D.G.B. performed theoretical analysis of the experimental data. B.M., D.G.B., and T.O.S. wrote the manuscript with input from all co-authors. T.O.S. supervised the study.

Competing interests The authors declare no competing interests.

Data and materials availability All data is available in the manuscript or the supplementary materials.

METHODS

Materials

Gold (III) chloride trihydrate ($\text{HAuCl}_4 \cdot 3\text{H}_2\text{O}$), L-ascorbic acid (AA), cetyltrimethylammonium bromide (CTAB) were purchased from Sigma-Aldrich for the synthesis of gold nanoflakes. For the synthesis of silver nanoflakes, silver nitrate (AgNO_3), sodium chloride (NaCl), polyvinyl pyrrolidone (PVP), ammonium hydroxide solution (NH_4OH , 25% w/w), and hydrogen peroxide solution (H_2O_2 , 30% w/w) were purchased from Sigma-Aldrich. All glassware and stir bars were thoroughly pre-cleaned and dried prior to use. Ultra-pure distilled water (Millipore, 18 $\text{M}\Omega\cdot\text{cm}$) was used in all preparations.

Synthesis of gold nanoflakes

Single crystalline gold nanoflakes were synthesized according to the literature [23]. In brief, using the rapid and seedless wet chemical method, 100 μL of 100 mM HAuCl_4 was added into 3 mL of 20 mM CTAB aqueous solution in a glass vial, and the mixture was gently mixed and left undisturbed for several minutes. Then, 100 μL of 100 mM AA was added to the mixture, followed by rapid inversion for 10 seconds. The resultant solution was immediately placed in a water bath of 85°C and kept undisturbed for about an hour. The products were washed by centrifugation at 4000 rpm for 10 min and finally dispersed in de-ionized water for further experiments.

Synthesis of silver nanoflakes

Single crystalline silver nanoflakes were selectively synthesized using the reduction of colorless silver ammine complex $[\text{Ag}(\text{NH}_3)_2]^+$ in the presence of Cl^- using H_2O_2 as a reducing agent [35]. Briefly, a colloid of AgCl nanoparticles was prepared by a rapid injection of 4 mL of 100 mM NaCl into a solution of 1 mL of 1M AgNO_3 and 10 mL of PVP (5% w/v) under vigorous stirring. A milky white colloid of AgCl nanoparticles spontaneously developed. The total volume was adjusted to 96 mL with DI water. The colloid was further stirred for 5 min before an addition of 1.7 mL of 5.3 M NH_4OH solution. The colloid became less opaque due to partial dissolution of AgCl nanoparticles with formation of a water soluble $[\text{Ag}(\text{NH}_3)_2]^+$ complex. To induce the formation of silver nanoflakes, 2.3 mL of H_2O_2 (30% w/w) was quickly injected into the colloid. The milky white colloid briefly turned into a sparkling glitter within 2 min by indicating the formation of silver nanoflakes. The colloid was further stirred for an hour to complete the reaction. The shiny silver precipitates were collected and washed 5 times by de-ionized water.

Sample preparation

All samples were prepared on thin microscope glass (170 μm) coverslips. The glass coverslips were cleaned in acetone and isopropanol at 60°C in ultrasonicator, dried with compressed nitrogen, followed by oxygen plasma cleaning. For the nanoflake dimer configuration, self-assembled Fabry-Pérot microcavities were formed between freely floating Au nanoflakes due to balance of Casimir and electrostatic forces, in a simple manner of drop casting an aqueous solution containing the Au nanoflakes onto glass coverslip. Then, the liquid was sealed with the PDMS O-ring and covered with a glass cover slip to prevent evaporation. It is noteworthy that the trimer samples were prepared from the diluted mixture solution of stock batch and de-ionized water with volume ratio of 1:1.

For nanoflake-on-static-mirror configuration, various thicknesses (10, 30, and 50 nm) of gold mirror was prepared by e-beam evaporator with adhesion layer of chromium (2 nm) to form the bottom mirror of the Fabry-Pérot microcavity. Then, various thicknesses of SiO_2 layer for half-cavities were deposited by sputtering on top of a freshly prepared bottom gold mirror, in order to tune the resonance of the cavity.

To fabricate the coupled polaritonic system, the several layer WSe₂ flakes were mechanically exfoliated from a crystal (HQ Graphene) and transferred on top of freshly-prepared half-cavities from the PDMS stamp using a dry-transfer technique [36]. Subsequently, aqueous solution containing the Au nanoflakes was drop-casted and liquid was sealed by the PDMS O-ring with a cover glass. The trapped and floating Au nanoflakes over the half-cavities with reflective bottom Au mirror form self-assembled Fabry-Pérot cavities and strongly couple with excitons in WSe₂.

Optical measurements

Reflection spectra at normal incidence (NA=0.5) were collected using an inverted microscope equipped with an oil-immersion 100× objective (switchable NA=0.5-1.3, Nikon), directed to a fiber-coupled spectrometer (Andor Shamrock SR-303i, equipped with a CCD detector Andor iDus 420). Dispersion relations in reflection were measured using NA=1.3 in the back-focal imaging setup using a fiber bundle. All reflectivity experiments were conducted under a collimated illumination with a laser-driven white light source (LDLS, EQ-99FC, high-brightness, flat-broadband spectrum).

To modulate the system in active manner, samples were illuminated from the top using a 100× long-working distance objective (NA=0.6) with mechanically chopped (4 Hz - 15 Hz) Continuous Wave (CW) ($\lambda = 455$ nm) laser. (see Fig. 4a) Simultaneously, time-resolved reflectivity spectra were recorded using an oil-immersion 100× objective (NA=0.5, Nikon), directed to a fiber-coupled spectrometer in Kinetic mode (Andor Shamrock SR-303i, equipped with a CCD detector Andor iDus 420). Note that a long-pass ($\lambda = 500$ nm) optical filter was installed in the detection path to block the modulating laser.

Casimir-electrostatic potential

The total ground state potential per unit area U_0 is the sum of the Casimir and electrostatic contributions. Casimir potential U_C of two gold mirrors in a solution was calculated using the Lifshitz framework [37]. The potential per unit area is obtained by the integration over the imaginary frequency $\omega = i\xi$ (with the parameter ξ acquiring real values):

$$U_C = \frac{\hbar}{2\pi} \int_0^\infty d\xi \int \frac{d^2\mathbf{k}_\parallel}{(2\pi)^2} \ln \det \mathbf{G} \quad (1)$$

where \mathbf{k}_{\parallel} is the in-plane component of the wave vector in the gap region of thickness L , $\mathbf{G} = \mathbf{1} - \mathbf{R}_1 \times \mathbf{R}_2 e^{-2K_0 L}$, and

$$\mathbf{R}_i = \begin{pmatrix} r_i^{ss} & 0 \\ 0 & r_i^{pp} \end{pmatrix} \quad (2)$$

is the reflection operator for i -th side of the system ($i = 1, 2$); r_i^q are the Fresnel reflection coefficients for i -th subsystem and polarization q evaluated at the imaginary frequency. $K_0 = \sqrt{\mathbf{k}_{\parallel}^2 + \xi^2/c^2}$ is the z-component of the wave vector in the gap between the two mirrors evaluated at the imaginary frequency.

The permittivity of gold at imaginary frequencies was evaluated with the Drude model $\varepsilon_{Au} = 8 - \omega_p^2/\omega(\omega + i\gamma)$ with $\omega_p = 8.6$ eV and $\gamma = 70$ meV approximating the Johnson and Christy experimental data [38].

The permittivity of water at imaginary frequencies ε_{H_2O} was evaluated by approximating the experimental data from ref. [39] with a series of Lorentzian transitions and a static Debye contribution:

$$\varepsilon(\omega) = \varepsilon_{\infty} + \frac{\varepsilon_D - \varepsilon_{\infty}}{1 - i\omega\tau} + \sum_{i=1}^3 f_i \frac{\omega_{P,i}^2}{\omega_{0,i}^2 - \omega^2 - i\gamma_i\omega} \quad (3)$$

where $\omega_{P,i}$ is the plasma frequency of i -th resonant transition, ω_0 and γ_i are the resonance frequency and linewidth, f_i the oscillator strength, ε_D is the amplitude of the Debye contribution, and τ is the Debye relaxation time of permanent dipoles. The resulting approximation of the complex-valued refractive index $n + i\kappa$ is shown in Fig. S6a. The analytical form of this expression allows us to evaluate the refractive index of water at the imaginary axis $n(i\xi)$, which takes purely real values and is presented in Fig. S6b.

Calculating the Casimir potential for two 30 nm thick Au films in water yields approximately L^n distance dependence of the potential with $n = -2.63$, Fig. S6. The slope being different from $n = -3$ predicted by the exact theory in the original Casimir effect stems from partial transparency of the mirrors.

The electrostatic potential per unit area U_e of two charged mirrors separated by the distance L in a solution with relative permittivity ε was estimated according to DLVO theory [3, 4]:

$$U_e = \frac{2\sigma^2}{\varepsilon_0\varepsilon(0)\kappa} e^{-\kappa L} \quad (4)$$

where $\kappa = \sqrt{\frac{\rho q_0^2 z^2}{\varepsilon(0)\varepsilon_0 k_B T}}$ is the inverse Debye-Hückel length, $\varepsilon(0)$ is the static permittivity of the solution (water), ρ is the density of ions with valence z , and σ is the surface charge

density of the plates.

Diffusion modelling

Stochastic dynamics of the vertical displacement z of a self-assembled cavity near equilibrium position in nanoflake dimer configuration was modelled by the Langevin equation with the noise term:

$$mz'' = -\gamma z' + F_{rest}(z) + \sqrt{2\gamma k_B T} f(t), \quad (5)$$

where z is the vertical displacement, m is the effective mass (twice the mass of a single flake), $F_{rest} = -AdU_0/dz$ is the restoring force, A is the surface area of the flake, γ is the friction coefficient, $f(t)$ is the white noise term with the correlator $\langle f(t)f(t') \rangle = \delta(t - t')$. Friction experienced by the flake upon its laminar motion in water can be described by Stokes' law: $\gamma = 6\pi\eta R$ where η is the viscosity, and R is the Stokes's radius of the flake. The Stokes's radius of the object is determined by many factors, and it can be further greatly affected by the close presence of the substrate (the boundary). Therefore, to make a reasonable assumption, we take the disk radius as a measure of its Stokes' radius R .

Analysis of modulated cavities

Empty modulated cavities were analyzed by the standard transfer-matrix method. The reflection spectra at each time instance were fitted by reflection coefficient at normal incidence calculated assuming 30 nm thick gold mirrors, 55 nm SiO₂ spacer with $n = 1.45$, and the solution refractive index of $n = 1.38$ consistent with other calculations.

Reflection spectra from the modulated coupled structures were analyzed with the Hamiltonian approach. Time-dependent positions of reflection dips were fitted with eigenvalues ω_{\pm} of the Jaynes-Cummings Hamiltonian:

$$\omega_{\pm} = (\omega_{cav} + \omega_0)/2 - i(\gamma_{cav} + \gamma_0)/4 \pm \sqrt{g^2 - (\omega_{cav} - \omega_0 + i(\gamma_{cav} - \gamma_0)/2)^2/4}, \quad (6)$$

where $\omega_{cav} - i\gamma_{cav}/2$ is the cavity complex eigenenergy, $\omega_0 - i\gamma_0/2$ is the exciton complex energy, g is the coupling strength. The cavity energy and the coupling strength were assumed to be modulated periodically with the triangular-like function (as suggested by the bare

cavity reflection spectra dynamics):

$$\omega_{cav}(t) = \omega_{cav,0} + \delta\omega_{cav}f(\Omega t + \phi) \quad (7)$$

$$g(t) = g_0 + \delta g f(\Omega t + \phi) \quad (8)$$

where Ω is the modulation frequency and $f(t)$ is the triangle wave:

$$f(t) = 4|t - \lfloor t + 1/2 \rfloor| - 1. \quad (9)$$

The cavity energy and the coupling strength modulation phases ϕ were assumed to be equal reflecting the fact that reducing cavity thickness increases the resonant energy, and increases the coupling constant at the same time.

The photonic and excitonic fractions of the polaritonic eigenstates are obtained as the corresponding elements of the Jaynes-Cummings Hamiltonian eigenvectors.

* timurs@chalmers.se

- [1] Casimir, H. B. On the attraction between two perfectly conducting plates. In *Proc. Kon. Ned. Akad. Wet.*, vol. 51, 793 (1948).
- [2] Rodriguez, A. W. *et al.* Classical and fluctuation-induced electromagnetic interactions in micron-scale systems: designer bonding, antibonding, and casimir forces. *Annalen der Physik* **527**, 45–80 (2015).
- [3] Derjaguin, B. V. & Landau, L. D. Theory of the stability of strongly charged lyophobic sols and of the adhesion of strongly charged particles in solutions of electrolytes. *Acta Physicochimica U.R.S.S.* **14**, 633–662 (1941).
- [4] Verwey, E. J. W. Theory of the stability of lyophobic colloids. *The Journal of Physical Chemistry* **51**, 631–636 (1947).
- [5] Lifshitz, E. M. The theory of molecular attractive forces between solids. *Soviet Phys. JETP* **2**, 73–83 (1956).
- [6] Dzyaloshinskii, I. E., Lifshitz, E. M. & Pitaevskii, L. P. The general theory of van der waals forces. *Advances in Physics* **10**, 165–209 (1961).
- [7] van Blokland, P. H. & Overbeek, J. T. G. Van der waals forces between objects covered with a chromium layer. *Journal of the Chemical Society, Faraday Transactions 1: Physical Chemistry in Condensed Phases* **74**, 2637–2651 (1978).

- [8] Lamoreaux, S. K. Demonstration of the casimir force in the 0.6 to 6 μ m range. *Physical Review Letters* **78**, 5 (1997).
- [9] Bressi, G., Carugno, G., Onofrio, R. & Ruoso, G. Measurement of the casimir force between parallel metallic surfaces. *Physical Review Letters* **88**, 041804 (2002).
- [10] Munday, J. N., Capasso, F. & Parsegian, V. A. Measured long-range repulsive casimir–lifshitz forces. *Nature* **457**, 170–173 (2009).
- [11] Batista, C. A. S., Larson, R. G. & Kotov, N. A. Nonadditivity of nanoparticle interactions. *Science* **350** (2015).
- [12] Lidzey, D. G. *et al.* Strong exciton–photon coupling in an organic semiconductor microcavity. *Nature* **395**, 53–55 (1998).
- [13] Khitrova, G., Gibbs, H., Kira, M., Koch, S. W. & Scherer, A. Vacuum rabi splitting in semiconductors. *Nature Physics* **2**, 81–90 (2006).
- [14] Törmä, P. & Barnes, W. L. Strong coupling between surface plasmon polaritons and emitters: a review. *Reports on Progress in Physics* **78**, 013901 (2014).
- [15] Dai, S. *et al.* Tunable phonon polaritons in atomically thin van der waals crystals of boron nitride. *Science* **343**, 1125–1129 (2014).
- [16] Basov, D., Fogler, M. & De Abajo, F. G. Polaritons in van der waals materials. *Science* **354**, aag1992 (2016).
- [17] Sidler, M. *et al.* Fermi polaron-polaritons in charge-tunable atomically thin semiconductors. *Nature Physics* **13**, 255–261 (2017).
- [18] Baranov, D. G., Wersäll, M., Cuadra, J., Antosiewicz, T. J. & Shegai, T. Novel nanostructures and materials for strong light-matter interactions. *ACS Photonics* **5**, 24 (2018).
- [19] Munkhbat, B. *et al.* Electrical control of hybrid monolayer tungsten disulfide–plasmonic nanoantenna light–matter states at cryogenic and room temperatures. *ACS Nano* **14**, 1196–1206 (2020).
- [20] Eichenfield, M., Camacho, R., Chan, J., Vahala, K. J. & Painter, O. A picogram-and nanometre-scale photonic-crystal optomechanical cavity. *Nature* **459**, 550–555 (2009).
- [21] Zhao, R. *et al.* Stable casimir equilibria and quantum trapping. *Science* **364**, 984–987 (2019).
- [22] Thomas, A. *et al.* Ground-state chemical reactivity under vibrational coupling to the vacuum electromagnetic field. *Angew. Chem. Int. Ed.* **55**, 11462–11466 (2016).
- [23] Chen, S. *et al.* Rapid seedless synthesis of gold nanoplates with microscaled edge length in a

- high yield and their application in sers. *Nano-micro letters* **8**, 328–335 (2016).
- [24] Li, R. *et al.* Study on the assembly structure variation of cetyltrimethylammonium bromide on the surface of gold nanoparticles. *ACS Omega* **5**, 4943–4952 (2020).
- [25] Liu, Y., Tourbin, M., Lachaize, S. & Guiraud, P. Silica nanoparticles separation from water: Aggregation by cetyltrimethylammonium bromide (ctab). *Chemosphere* **92**, 681–687 (2013).
- [26] Meena, S. K. *et al.* The role of halide ions in the anisotropic growth of gold nanoparticles: a microscopic, atomistic perspective. *Physical Chemistry Chemical Physics* **18**, 13246–13254 (2016).
- [27] Chen, F., Mohideen, U., Klimchitskaya, G. & Mostepanenko, V. Demonstration of the lateral casimir force. *Physical Review Letters* **88**, 101801 (2002).
- [28] Chen, F., Mohideen, U., Klimchitskaya, G. & Mostepanenko, V. Experimental and theoretical investigation of the lateral casimir force between corrugated surfaces. *Physical Review A* **66**, 032113 (2002).
- [29] Rodrigues, R. B., Neto, P. A. M., Lambrecht, A. & Reynaud, S. Lateral casimir force beyond the proximity-force approximation. *Physical Review Letters* **96**, 100402 (2006).
- [30] Meyer, M., Le Ru, E. & Etchegoin, P. Self-limiting aggregation leads to long-lived metastable clusters in colloidal solutions. *The Journal of Physical Chemistry B* **110**, 6040–6047 (2006).
- [31] Baranov, D. G. *et al.* Ultrastrong coupling between nanoparticle plasmons and cavity photons at ambient conditions. *Nature Communications* **11**, 2715 (2020).
- [32] Junginger, A. *et al.* Tunable strong coupling of two adjacent optical $\lambda/2$ fabry-pérot microresonators. *Optics Express* **28**, 485–493 (2020).
- [33] Berkhout, A., Wolterink, T. A. & Koenderink, A. F. Strong coupling to generate complex birefringence-metasurface in the middle etalons. *ACS Photonics* **7**, 2799 (2020).
- [34] Li, Y. *et al.* Measurement of the optical dielectric function of monolayer transition-metal dichalcogenides: MoS_2 , MoSe_2 , WS_2 , and WSe_2 . *Physical Review B* **90**, 205422 (2014).
- [35] Gatemala, H., Pienpinijtham, P., Thammacharoen, C. & Ekgasit, S. Rapid fabrication of silver microplates under an oxidative etching environment consisting of O_2/Cl^- , $\text{NH}_4\text{OH}/\text{H}_2\text{O}_2$, and H_2O_2 . *CrystEngComm* **17**, 5530–5537 (2015).
- [36] Castellanos-Gomez, A. *et al.* Deterministic transfer of two-dimensional materials by all-dry viscoelastic stamping. *2D Materials* **1**, 011002 (2014).
- [37] Lifshitz, E. M., Hamermesh, M. *et al.* The theory of molecular attractive forces between solids.

In *Perspectives in Theoretical Physics*, 329–349 (Elsevier, 1992).

- [38] Johnson, P. B. & Christy, R.-W. Optical constants of the noble metals. *Physical review B* **6**, 4370 (1972).
- [39] Segelstein, D. The complex refractive index of water, master's thesis. *University of Missouri* (1981).

Figures

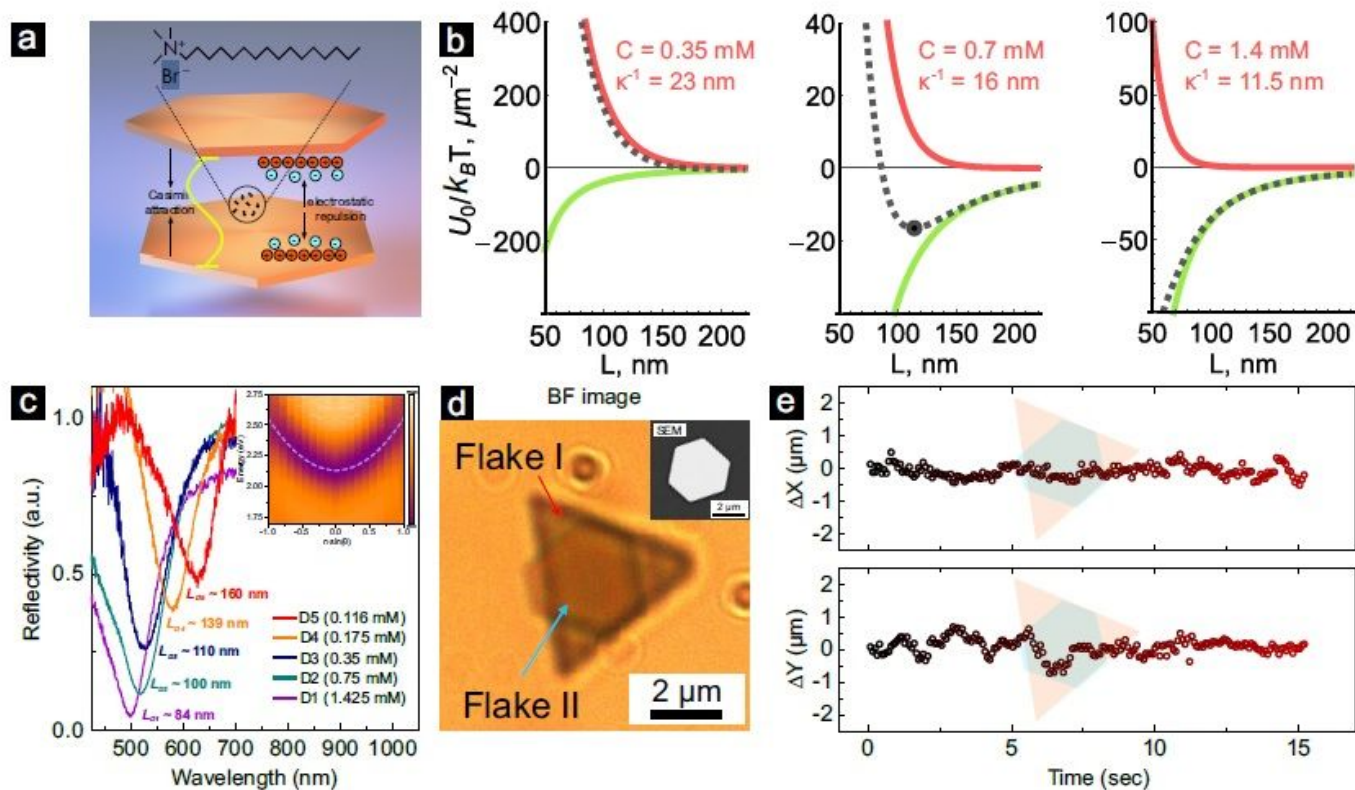


Figure 1

The self-assembled microcavity system and the physical mechanism behind its operation. (see Manuscript file for full figure legend)

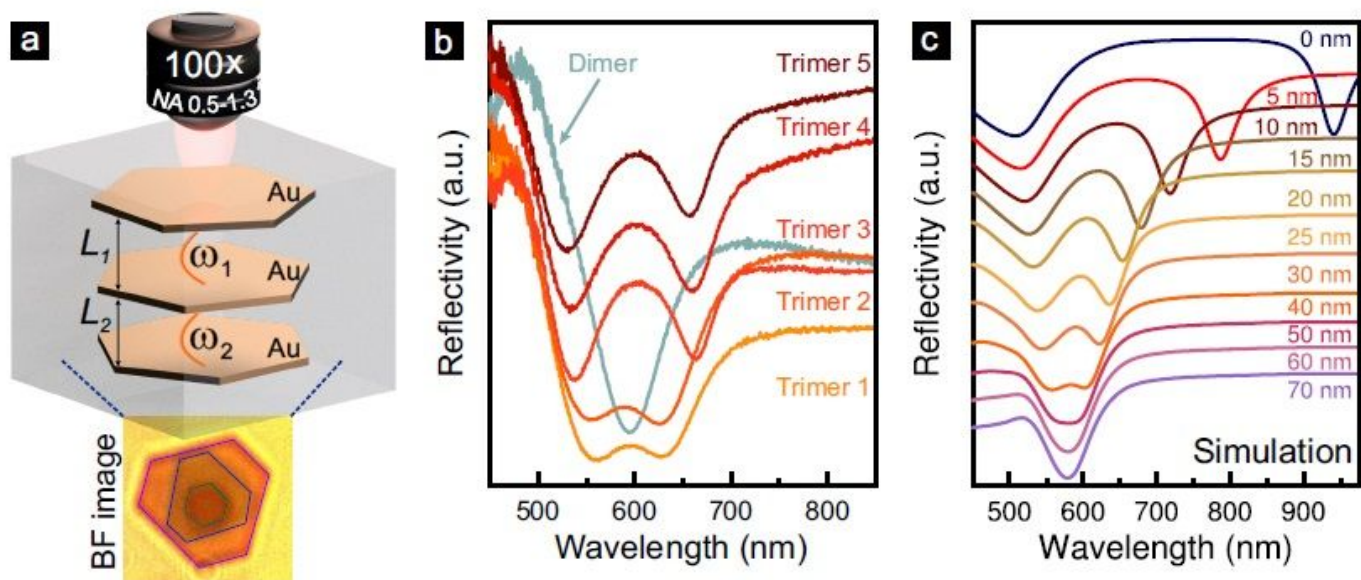


Figure 2

Self-assembled trimer cavities. (see Manuscript file for full figure legend)

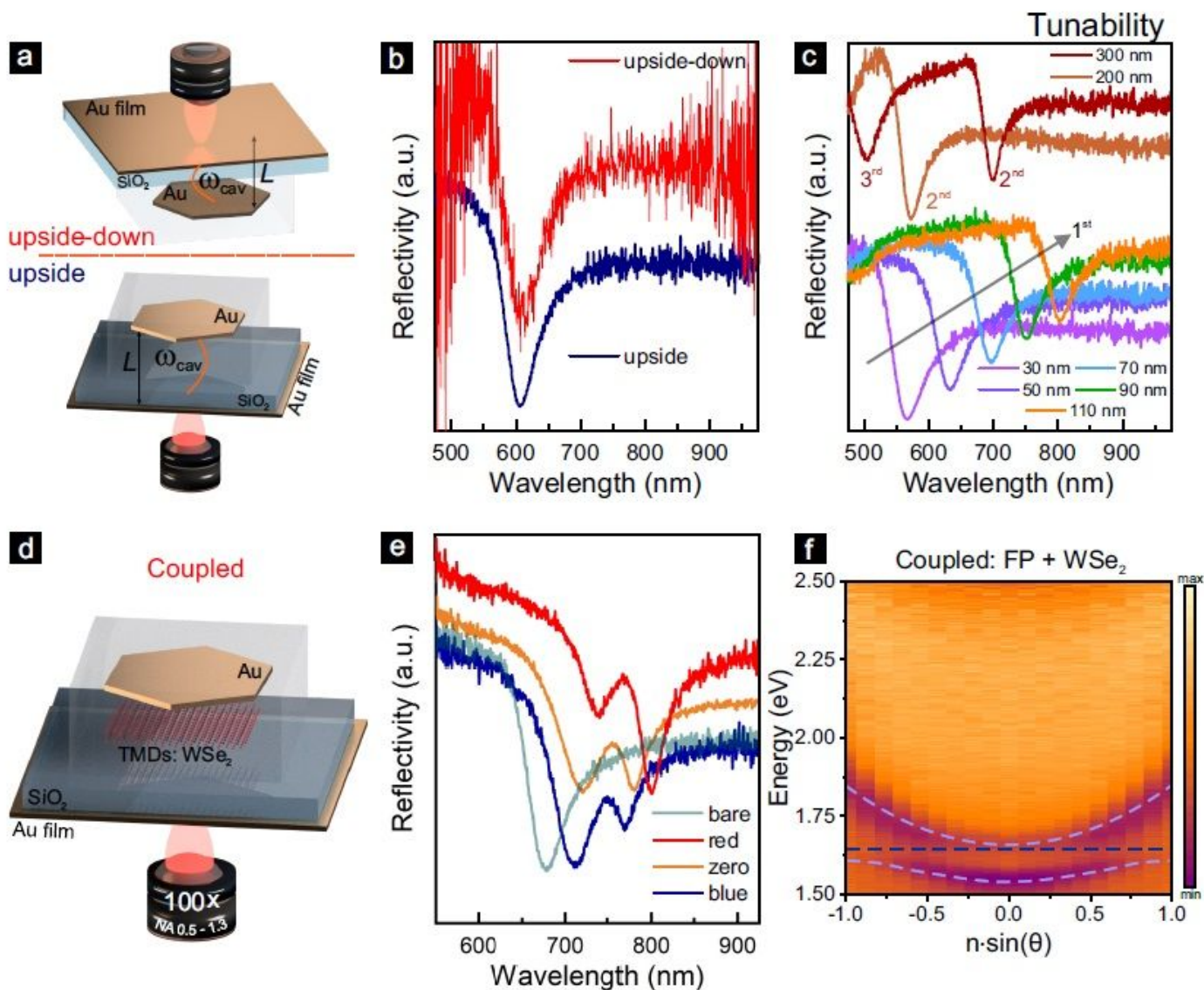


Figure 3

Self-assembled cavities in nanoflake-on-static-mirror configuration and the formation of polaritons. (see Manuscript file for full figure legend)

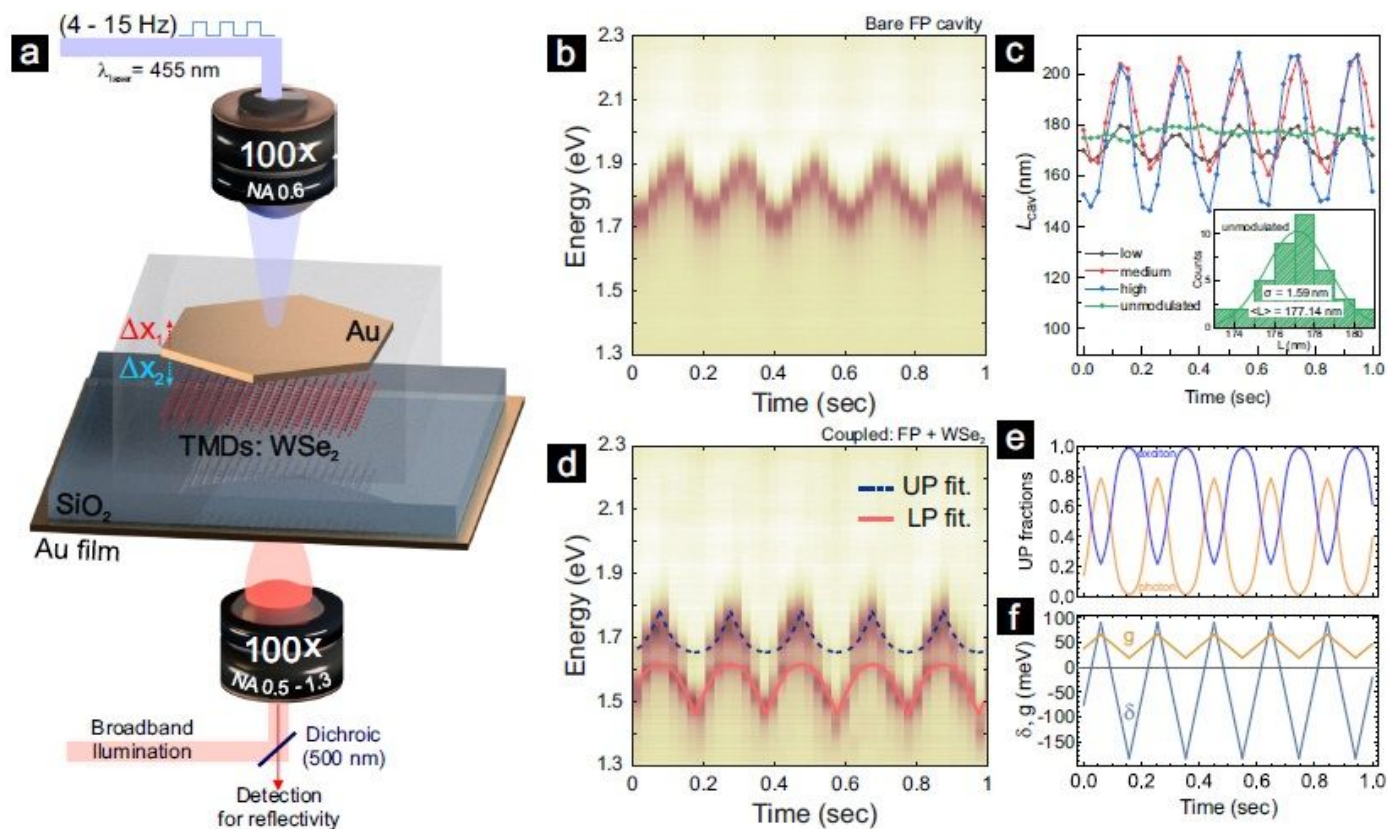


Figure 4

Actively tunable microcavities and polaritons. (see Manuscript file for full figure legend)

Supplementary Files

This is a list of supplementary files associated with this preprint. Click to download.

- [SITunableCasimirNaturefinal.pdf](#)
- [MovieS1.mp4](#)
- [MovieS2.mp4](#)
- [MovieS3.mp4](#)
- [MovieS4.mp4](#)
- [MovieS5.mp4](#)
- [MovieS6.mp4](#)